

Swin Deformable Attention Hybrid U-Net for Medical Image Segmentation

Lichao Wang
 Jiahao Huang
 Guang Yang

L.WANG22@IMPERIAL.AC.UK
 J.HUANG21@IMPERIAL.AC.UK
 G.YANG@IMPERIAL.AC.UK *Address*

Editors: Under Review for MIDL 2023

Abstract

How to harmonize convolution and multi-head self-attention mechanisms has recently emerged as a significant area of research in the field of medical image segmentation. Various combination methods have been proposed. However, there is a common flaw in these works: failed to provide a direct explanation for their hybrid model, which is crucial in clinical scenarios. Deformable Attention can improve the segmentation performance and provide an explanation based on the deformation field. Incorporating Deformable Attention into a hybrid model could result in a synergistic effect to boost segmentation performance while enhancing the explainability. In this study, we propose the incorporation of Swin Deformable Attention with hybrid architecture to improve the segmentation performance while establishing explainability. In the experiment section, our proposed Swin Deformable Attention Hybrid UNet (SDAH-UNet) demonstrates state-of-the-art performance on both anatomical and lesion segmentation tasks.

Keywords: Medical image segmentation, Transformer, CNN, XAI, Deformable Attention

1. Introduction

Semantic segmentation is an integral part of medical image analysis. Robust and accurate medical image segmentation could be of great help in many clinical scenarios. For instance, gliomas are the most common malignant brain tumors with different levels of aggressiveness. Automated and accurate segmentation of these malignancies on magnetic resonance imaging (MRI) is of vital importance for clinical diagnosis (Wang et al., 2021). Recently, many research studies focused on harmonizing convolution and multi-head self-attention mechanisms (MSA) together to boost the segmentation performance (Chen et al., 2021; Xu et al., 2021; Wang et al., 2021; Hatamizadeh et al., 2021; Park and Lee, 2022; Sun et al., 2021; Guo et al., 2022; Liu et al., 2022a). Despite the contributions of these works, a prevalent shortcoming is the lack of a clear and direct explanation for the hybrid models.

To provide explanation for deep learning models, the gradient and feature map based explanation approaches like the Gradient-weighted Class Activation Mapping (Grad-CAM) (Selvaraju et al., 2016) and Layer-Wise Relevance Propagation (Bach et al., 2015) can offer heatmap to indicate which neurons the model focuses on; however, these approaches fall short in giving further explanation about why the model can pay more attention to these areas. Another commonly used method for explaining the MSA-based model is the visualization of attention score heatmaps for a specific query. The attention score heatmaps are based on patches, limiting the resolution of the heatmaps.

In this study, we first use Grad-CAM to analyze the current state-of-the-art hybrid model, i.e., UNet-2022, whose basic block is designed in a parallel paradigm. The gradient heatmaps show that the SMSA-branch focuses more on the pixels inside the boundary of the target and delineates a more precise contour. Intuitively, this unique feature is derived from the data-specificity nature of MSA (Park and Kim, 2022). On the other hand, the Conv-branch is able to retain the model’s focus on

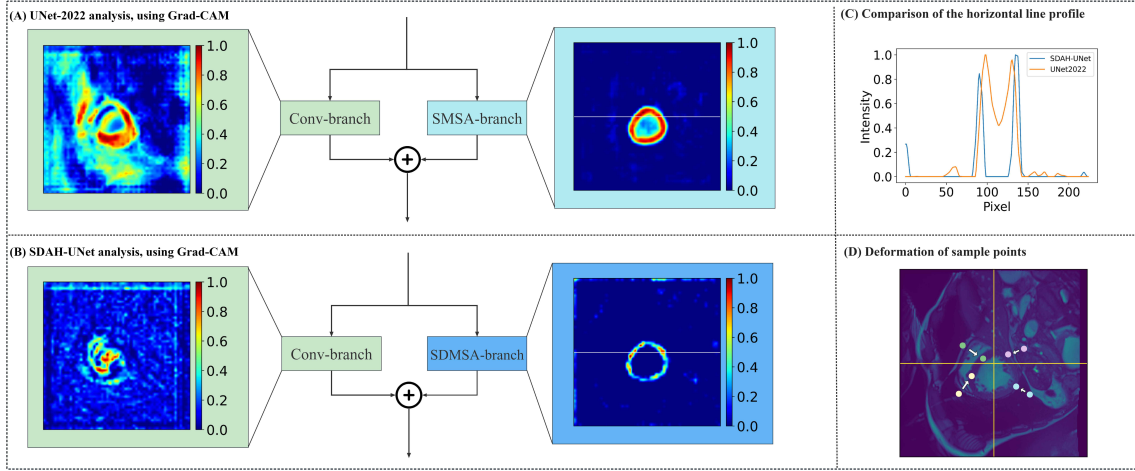


Figure 1: Analysis of UNet-2022 and SDAH-UNet. In panel (A) and (B), we present the gradient heat maps (Selvaraju et al., 2016) of two branches in the basic block of UNet-2022, and SDAH-UNet. In panel (C), we show the comparison of horizontal line profiles in SMSA and SDMSA-branch. Panel (D) briefly displays the deformation of the sample points in the SDMSA module. SMSA represents the Swin Multi-head Self-Attention, and SDMSA represents the Swin Deformable Multi-head Self-Attention.

the major foreground area, attributed to the local information-acquiring ability of the convolutional layer.

To enhance the performance and provide further explanation, one intuitive way is to improve the precise delineation ability of the Swin Multi-head Self-Attention branch (SMSA-branch). Deformable Attention can limit the focus of the model on certain locations and provide the explanation based on its deformation field (Xia et al., 2022). Based on this analysis, we develop a novel hybrid block containing a Swin Deformable MSA (SDMSA) module (Huang et al., 2022) (Figure 1 (D)), aiming at further improving the SMSA-branch’s ability on delineating precise contours and preventing high computational cost, with a parallel convolutional branch. According to the gradient heatmap (Figure 1 (A), (B)) and the line profile of the SMSA-branch and SDMSA-branch (Figure 1 (D)), the Swin Deformable MSA module enables our proposed model to focus more accurately on the segmentation targets. We further leverage the deformation of the sample points to provide a more complete explanation of the model, both in terms of the focalization and how the model forms the focalization.

We hypothesize that (1). our proposed model can achieve state-of-the-art performance on multiple medical image segmentation datasets, incorporating different clinical questions; (2). the SDMSA module enables the model to focus more precisely on the segmentation targets and provides explainability. Our contributions are listed as follows: (1). we propose a Swin Deformable Attention Hybrid UNet (SDAH-UNet) model for medical image segmentation; (2). our SDMSA with parallel convolution (SDAPC) block improves the segmentation performance based on the Swin Deformable Attention which strengthens the model’s focus on the segmentation targets and can provide explanations; (3). In the experiment section, SDAH-UNet significantly outperforms state-of-the-art models, on automatic cardiac diagnosis challenge (Bernard et al., 2018) (ACDC), and brain tumor segmentation 2020 (Menze et al., 2015) (BraTS2020).

2. Methodology

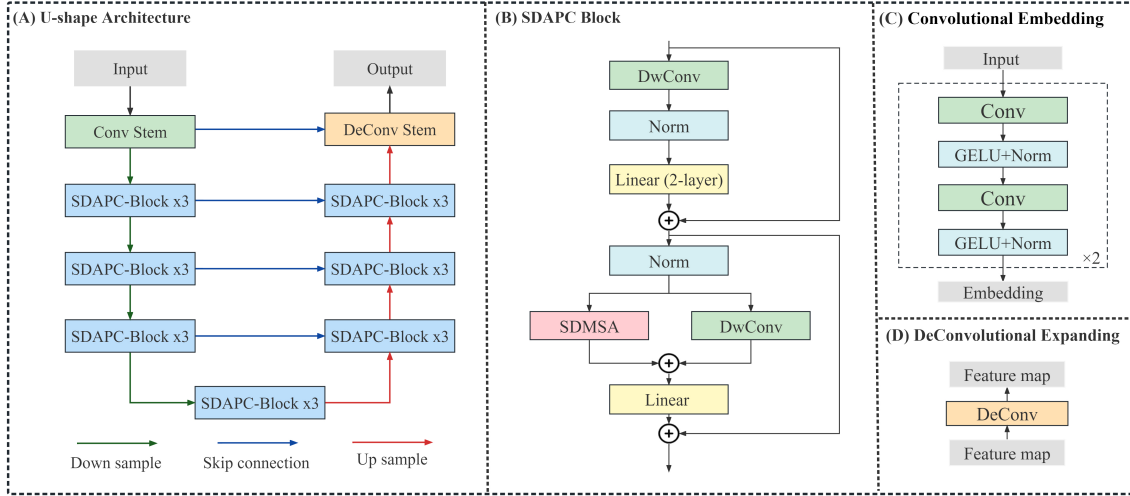


Figure 2: The illustration of Swin Deformable Attention Hybrid UNet (SDAH-UNet). Part (A) illustrates the overall architecture of SDAH-UNet. Part (B) displays the proposed SDMSA with parallel convolution (SDAPC) block. In part (C) and part (D), Convolutional Embedding and DeConvolutional Expanding modules are presented.

2.1. U-Shape Architecture

Our model is an end-to-end model that takes an image slice as input and produces a segmentation mask as output. The proposed model follows a symmetrical design paradigm, with both the encoder and decoder consisting of three SDAPC blocks. A convolutional stem is added at the beginning of the encoder, a deconvolutional stem is added at the end of the decoder, and an additional SDAPC block is inserted in the bottleneck (Figure 2 (A)).

2.2. Convolutional Embedding Module and DeConvolutional Expanding Module

Inspired by recent studies (Zhou et al., 2021; Guo et al., 2022), we directly use successive convolutional layers with small kernels as the embedding module. This modification aims to precisely encode pixel-level spatial information while reducing computational complexity and maintaining a large receptive field. The embedding module comprises four convolutional layers, with one GELU and one layer normalization layer following each convolutional layer. The expanding module is a deconvolutional layer (Figure 2 (C) and (D)). This simple stack can be extended to accommodate higher-resolution inputs.

2.3. Swin Deformable Multi-head Self-Attention with Parallel Convolution Block

Multi-head Self-Attention and convolution have been shown to have distinct weighting mechanisms (Guo et al., 2022), filtering effects (Park and Kim, 2022), and levels of focus on feature map details, which complement each other. In order to leverage the advantages of both, our SDAPC block is designed in a parallel paradigm and employs Deformable Attention to further enhance the precise delineation capability of the MSA (Figure 2 (B)). Partitioned by the two residual connections, the

SDAPC block has two divisions. In the first division, the input X first passes a DwConv layer, $\text{DwConv}(\cdot)$, then passes a standard 2-layer multi-layer perceptron (MLP), which can be described as

$$\bar{X} = \text{FC}_2(\text{GELU}(\text{FC}_1(\text{LN}(\text{DwConv}(X)))) + X, \quad (1)$$

in which $\text{FC}_1(\cdot)$ and $\text{FC}_2(\cdot)$ are full connection layers. $\text{GELU}(\cdot)$ and $\text{LN}(\cdot)$ denote the GELU and Layer Normalization layers.

In the second division, \bar{X} is passed to the paralleled DwConv layer, $\text{DwConv}(\cdot)$, and Swin Deformable MSA layer, $\text{SDMSA}(\cdot)$, whose outputs are concatenated together and passed through the last FC layer. Inspired by the design of ConvNeXt (Liu et al., 2022b), our DwConv’s kernel size is set as 7. The process can be described as

$$\hat{X} = \text{FC}(\text{SDMSA}(\text{LN}(\bar{X})) + \text{DwConv}(\text{LN}(\bar{X}))) + \bar{X}, \quad (2)$$

in which SDMSA stands for the Swin Deformable Multi-head Self-Attention.

2.4. Shifted Windows Deformable Multi-head Self-Attention

Followed by the Deformation Attention Transformer (Xia et al., 2022) and the Swin Deformable Attention U-Net Transformer (Huang et al., 2022), we change the Swin MSA into the Swin Deformable MSA. The input feature map $F \in \mathbb{R}^{N \times W \times H}$ are first split into N_w non-overlapping windows and then divided into N_h heads along the channels. After the partition, $N_w \times N_h$ sub-feature maps are generated, where $N_w = WH/W_s^2$, W_s stands for window size. For a sub-feature map F_i^j , where i and j represent the i^{th} window and the j^{th} head respectively, we calculate the query q_i^j , and set up a group of uniformly distributed reference sample points p_i^j . The reference sample points are added with the offsets Δp_i^j obtained from a two-layer convolutional network $\text{CNN}_{\text{offest}}(\cdot)$, to generate the deformed sample points $p_i^j + \Delta p_i^j$. A bilinear interpolation function $\phi(\cdot)$ is used to generate the sampled features. Then keys and values are calculated based on the sampled features. The Swin Deformable MSA can be presented as follows

$$q_i^j = F_i^j W_{Q_i}^j, \quad \Delta p_i^j = \text{CNN}_{\text{offest}}(q_i^j), \quad (3)$$

$$\hat{F}_i^j = \phi(F_i^j; p_i^j + \Delta p_i^j), \quad k_i^j = \hat{F}_i^j W_{K_i}^j, \quad v_i^j = \hat{F}_i^j W_{V_i}^j, \quad (4)$$

$$Z_i^j = \text{SoftMax}(q_i^j k_i^j / \sqrt{d} + b_i^j) v_i^j, \quad (5)$$

where $W_{Q_i}^j$, $W_{K_i}^j$, and $W_{V_i}^j$ are the projection matrices for queries, keys, and values, respectively. b_i^j represents the fixed positional bias (Liu et al., 2021). The dimension of each head is represented as $d = C/N_h$, where C is the number of output channels and N_h is the number of heads.

3. Experiments

Experiments were conducted on two medical image segmentation tasks, ACDC, and BraTS2020, which incorporate different clinical questions and various MRI sequences to validate the efficacy of our proposed methods. ACDC is an anatomical segmentation task, with one MRI sequence serving as the input. BraTS2020 is a lesion segmentation task, with four MRI sequences as input. MRI volumetric data was split into slices for the model training.

3.1. Implementation Details and Evaluation Methods

We conducted our experiments on an NVIDIA RTX3090 GPU with 24GB GPU RAM. Dice loss $\mathcal{L}_{\text{dice}}$ and cross-entropy loss \mathcal{L}_{CE} were combined as the loss function

$$\mathcal{L} = \mathcal{L}_{\text{dice}} + \mathcal{L}_{\text{CE}}. \quad (6)$$

In the training process, the batch size and input resolution were set to 24 and 224×224 for all datasets. The initial learning rate was set to 2×10^{-4} and decayed every 10,000 steps by 0.5 from the 50,000th step. During the inference stage, our model makes predictions using a sliding window approach (Isensee et al., 2018). On the two datasets, we set 112, 0.5 times of the crop size (224), as the step size. For patch aggregation, the Gaussian importance weighting strategy was utilized, giving more weight to pixels in the center area.

3.2. Datasets

The ACDC dataset (Bernard et al., 2018) contains 100 cine MRIs (1,902 slices) of patients who have been clinically diagnosed in five classes: normal, dilated cardiomyopathy (DCM), hypertrophic cardiomyopathy (HCM), heart failure with infarction (MINF), or right ventricular abnormality (RVA). In the experimental setup, the dataset was randomly divided into a training set (70 cases, 1,290 slices), a validation set (10 cases, 196 slices), and a test set (20 cases, 416 slices). For each patient, short axis (SA) cine MRI with 12-35 frames is available, in which the end-diastole (ED) and end-systole (ES) frames have been indicated. The dataset contains three foreground classes for labels: right ventricle, myocardium, and left ventricle, which are served as the segmentation targets.

The BraTS2020 dataset (Menze et al., 2015) is composed of 369 cases (57,195 slices). In the experimental setup, the dataset was randomly partitioned into three subsets: a training set (229 cases and 35,495 slices), a validation set (70 cases and 25,830 slices), and a test set, (70 cases and 25,830 slices). Each case is composed of four modalities of brain magnetic resonance imaging (MRI) scans, specifically native T1-weighted, post-contrast T1-weighted, T2-weighted, and Fluid Attenuated Inversion Recovery scans. Each modality has a volume of $240 \times 240 \times 155$, which have been aligned into the same space. The dataset contains four distinct classes for labels: background (label 0), necrotic and non-enhancing tumor (label 1), peritumoral edema (label 2), and GD-enhancing tumor (label 4). The segmentation accuracy is evaluated for the enhancing tumor region (ET, label 1), regions of the tumor core (TC, labels 1 and 4), and the whole tumor region (WT, labels 1,2, and 4).

Dice score (DSC) and 95% Hausdorff distance (HD95) were used as evaluation metrics.

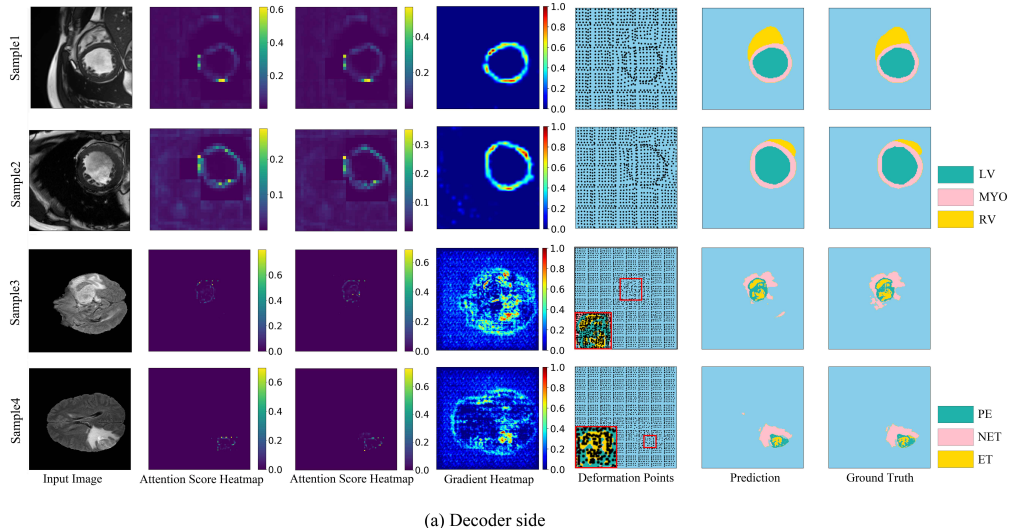
3.3. Comparison Studies

Methods	DSC		DSC		
	AVG	HD95	RV	MYO	LV
UNet	87.68	1.55	$83.82 \pm 11.04^\dagger$	$84.21 \pm 9.97^\dagger$	$95.04 \pm 5.09^\dagger$
nnUNet	91.86	1.22	88.86 ± 7.43	89.77 ± 2.29	96.97 ± 0.75
SwinUNet	88.08	1.61	$85.24 \pm 8.48^\dagger$	$84.45 \pm 7.76^\dagger$	$94.56 \pm 4.64^\dagger$
UNet-2022	90.42	1.41	$87.36 \pm 9.09^\dagger$	$87.78 \pm 5.09^\dagger$	$96.13 \pm 3.28^\dagger$
SDAH-UNet	92.23	1.22	89.78 ± 9.97	90.02 ± 4.23	96.91 ± 1.91

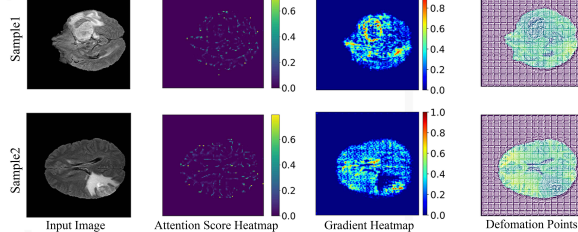
Table 1: Comparison with state-of-the-art MSA-based, Convolution-based, and hybrid models on the ACDC dataset. † : $p < 0.05$ (using paired sample t-test). RV: Right Ventricle, MYO: Myocardium, LV: Left Ventricle

Methods	DSC	HD95	DSC		
	AVG	WT	TC	ET	
UNet	82.27	9.04	$85.68 \pm 8.82^\dagger$	$85.46 \pm 8.67^\dagger$	$75.69 \pm 8.92^\dagger$
nnUNet	83.64	<u>4.30</u>	$86.45 \pm 10.89^\dagger$	$82.35 \pm 7.28^\dagger$	$82.13 \pm 11.37^\dagger$
SwinUNet	84.56	9.25	$87.47 \pm 7.10^\dagger$	$85.50 \pm 9.08^\dagger$	$80.71 \pm 8.04^\dagger$
UNet-2022	84.76	5.52	$87.95 \pm 9.03^\dagger$	$85.97 \pm 9.61^\dagger$	$80.35 \pm 8.68^\dagger$
SDAH-UNet	86.90	3.65	90.21 ± 3.55	88.13 ± 5.23	82.37 ± 5.45

Table 2: Comparison with state-of-the-art MSA-based, Convolution-based, and hybrid models on the BraTS2020 dataset. † : $p < 0.05$ ((using paired sample t-test). ET: Enhanced Tumor, TC: Tumor Core, WT: Whole Tumor



(a) Decoder side



(b) Encoder side

Figure 3: Visual explanation for SDAH-UNet. For decoder, the Attention Score Heatmap, Gradient Heatmap, Deformation Points, and Deformation Field are captured from the last block, with down sampling process for the deformation points. For encoder, all figures are captured from the first block, without down sampling process. LV, MYO, and RV stand for left ventricle, myocardium, and right ventricle; PE, NET, and ET stand for peritumoral edema, necrotic and non-enhancing tumor, and GD-enhancing tumor

The quantitative results of the comparison on two general medical image segmentation datasets are reported in Tables 1, and 2. Results demonstrate that (1). On ACDC, the proposed model outperforms state-of-the-art model, nnUNet, with superior mean DSC on ACDC but no statisti-

cal significance, and, on BraTS2020, the proposed model significantly outperforms state-of-the-art model, UNet-2022, with superior DSC and HD95 on BraTS2020; (2). the proposed SDAH-UNet, with strong generalization ability, can be applied to multiple datasets including anatomical and lesion segmentation datasets.

The visual explanations for decoder and encoder are shown Fig. 3. For the ACDC dataset, it has been observed that all the visual explanation methods are capable of illustrating the decoder’s focalization. Although the deformation of sample points impaired the visualization of the feature map, the outline of the myocardium could still be viewed. For a more challenging task, BraTS2020, the attention score heatmap could only provide a general indication of the tumor location, and the gradient heatmap had excessive highlight areas. In contrast, the utilization of deformation points has presented a clearer representation of the model’s focalization. The analysis of global area results further supports this finding, as it revealed that only sample points that were sufficiently close to the tumor exhibit deformation and were clustered in the tumor area. Additionally, when examining the results in a zoomed-out window, it could be observed that within the whole tumor area, sample points were concentrated in the enhanced tumor area. For the encoder, the attention score heatmap was found to only depict the approximate location of the tumor without providing any additional information. The gradient heatmap has shown that, in sample 1, the model paid more attention to the highlighted area; however, for sample 2 the gradient heatmap has shown that the model ignores the highlighted tumor area. On the other hand, the deformation points illustrated that the model focused on both the highlighted areas and the boundaries.

This outcome supports the hypothesis that, comparing to other visual explanation methods, the deformation points can facilitate a better understanding of the focalization, as well as the underlying mechanism that drives the formation of focalization in the model.

3.4. Ablation Studies

We set two ablation studies to investigate the influence of the number of the SDAPC blocks and the two parallel branches of the SDAPC block.

Table. 3 shows that the performance of the model improved when the non-isomorphic block (NI-block) was gradually replaced by the SDAPC block. replacing the first NI-block with the SDAPC block lead to nearly 1.2% performance enhancement for DSC. However, continuing to replace the NI-blocks could not have a significant influence. Table. 4 illustrates that removing each branch from the SDAPC block leads to a decline in performance, nearly 2% DSC.

Methods	DSC	HD95	DSC		
	AVG		RV	MYO	LV
NNNN	90.42	1.41	87.36 ± 9.09	87.78 ± 5.09	96.13 ± 3.28
DNNN	91.61	1.22	89.30 ± 5.80	88.79 ± 2.82	96.74 ± 0.88
DDNN	91.86	1.23	89.87 ± 5.34	88.88 ± 3.10	96.83 ± 0.87
DDDN	91.99	1.22	90.02 ± 6.21	89.35 ± 3.01	96.61 ± 1.83
DDDD	92.23	1.22	89.78 ± 9.97	90.02 ± 4.23	96.91 ± 1.91

Table 3: Comparison of the different numbers of SDAPC blocks adopted in the model on the ACDC dataset. ‘N’ stands for the NI block (the hybrid block used in UNet-2022), and ‘D’ stands for the SDAPC block.

Branch Type	DSC	HD95	DSC		
	AVG		RV	MYO	LV
SDMSA-branch	90.48	1.45	87.35 ± 5.73	88.53 ± 2.12	95.58 ± 1.11
Conv-branch	90.26	1.98	87.06 ± 6.41	88.35 ± 3.25	95.38 ± 1.32
Dual-branch	92.23	1.22	89.78 ± 9.97	90.02 ± 4.23	96.91 ± 1.91

Table 4: Comparison of the two branches of SDAPC block on the ACDC dataset. SDMSA-branch stands for the basic block of the model has the only Swin Deformable MSA branch. Conv-branch stands for the basic block of the model has the only convolutional branch. Dual branch stands for the proposed model.

4. Discussion and Conclusion

In this work, we have developed the Swin Deformable MSA with parallel convolution block, i.e., SDAPC block, and proposed the Swin Deformable Attention Hybrid UNet, i.e., SDAH-UNet, for explainable medical image segmentation. The experiments have proven that:

(1) SDAH-UNet outperforms the state-of-the-art model, nnUNet, nearly 0.5% mean DSC on ACDC but no statistical significance, and UNet-2022, over 2% DSC on BraTS2020 with statistical significance. The ablation studies have illustrated that both the SDMSA module and the parallel convolution layer improved the hybrid model’s performance.

(2) The deformation points can illustrate the model’s focalization, and how the model forms the focalization. The explanations have also proven that the SDAPC block enables the model to focus more precisely on the segmentation targets, based on its deformation mechanism, and leads to performance enhancement.

In the ablation study of SDAPC block numbers, replacing the first NI-block with the SDAPC block resulted in a nearly 1.2% performance enhancement for DSC. However, further replacement of NI-blocks did not have a significant impact. This may be due to the uneven distribution of information within the input image. Utilizing Deformable Attention allows the model to selectively focus on regions of higher information density, but the patch merging operation balances the distribution of information within deeper feature maps. Thus, increasing the number of SDAPC blocks may not significantly improve performance.

In the visual explanation, the attention score heatmap is able to indicate the model’s focalization on the ACDC dataset. However, when applied to the BraTS2020 dataset, the heatmap appears to be extremely sparse and vague. This result may be due to the wider distribution of deformation points for the BraTS2020 dataset, impairing alignment of the attention score heatmap and corresponding feature map. The gradient heatmap can demonstrate the model’s focalization for the ACDC dataset. However, for the BraTS2020 dataset, unrelated areas are also being focused. This may be caused by the cerebrospinal fluid (CSF) which is also highlighted in the input image and falsely treated as the tumor area by the decoder. From the deformation points, we can clearly see the myocardium for ACDC. In the case of the BraTS2020 dataset, on the decoder side, the sample points are deformed to cover the entire tumor area in the global view, and within the tumor area, the sample points are concentrated in the enhanced tumor region and the boundary of the peritumoral edema. On the encoder side, it can be observed that the sample points are gathered in highlighted regions and boundaries. This outcome suggests that the sample points tend to migrate towards the most information-dense region, assisting the decoder to focus on the important features already generated in the previous layer, and the encoder in extracting more information from potential target regions on the input image, however, it also amplifies the negative influence of some ambiguous areas, such as the cerebrospinal fluid in the brain, which can lead to erroneous predictions.

Acknowledgments

We thank a bunch of people.

References

Sebastian Bach, Alexander Binder, Grégoire Montavon, Frederick Klauschen, Klaus-Robert Müller, and Wojciech Samek. On Pixel-Wise Explanations for Non-Linear Classifier Decisions by Layer-Wise Relevance Propagation. *PLoS ONE*, 10, 2015.

Olivier Bernard, Alain Lalande, Clément Zotti, Frédéric Cervenansky, Xin Yang, Pheng-Ann Heng, Irem Cetin, Karim Lekadir, Oscar Camara, Miguel A. González Ballester, Gerard Sanromá, Sandy Napel, Steffen Erhard Petersen, Georgios Tziritas, Elias Grinias, Mahendra Khened, Varghese Alex Kollerathu, Ganapathy Krishnamurthi, Marc-Michel Rohé, Xavier Pennec, Maxime Sermeasant, Fabian Isensee, Paul F. Jäger, Klaus Maier-Hein, Peter M. Full, Ivo Wolf, Sandy Engelhardt, Christian F. Baumgartner, Lisa M. Koch, Jelmer M. Wolterink, Ivana Iýsgum, Yeonggul Jang, Yoonmi Hong, Jay Patravali, Shubham Jain, Olivier Humbert, and Pierre-Marc Jodoin. Deep Learning Techniques for Automatic MRI Cardiac Multi-Structures Segmentation and Diagnosis: Is the Problem Solved? *IEEE Transactions on Medical Imaging*, 37:2514–2525, 2018.

Jieneng Chen, Yongyi Lu, Qihang Yu, Xiangde Luo, Ehsan Adeli, Yan Wang, Le Lu, Alan Loddon Yuille, and Yuyin Zhou. TransUNet: Transformers Make Strong Encoders for Medical Image Segmentation. *ArXiv*, abs/2102.04306, 2021.

Jiansen Guo, Hong-Yu Zhou, Liansheng Wang, and Yizhou Yu. UNet-2022: Exploring Dynamics in Non-isomorphic Architecture. 10 2022.

Ali Hatamizadeh, Dong Yang, Holger R. Roth, and Daguang Xu. UNETR: Transformers for 3D Medical Image Segmentation. *2022 IEEE/CVF Winter Conference on Applications of Computer Vision (WACV)*, pages 1748–1758, 2021.

Jiahao Huang, Xiaodan Xing, Zhifan Gao, and Guang Yang. Swin Deformable Attention U-Net Transformer (SDAUT) for Explainable Fast MRI. In *International Conference on Medical Image Computing and Computer-Assisted Intervention*, 2022.

Fabian Isensee, Jens Petersen, Andre Klein, David Zimmerer, Paul F. Jaeger, Simon Kohl, Jakob Wasserthal, Gregor Koehler, Tobias Norajittra, Sebastian Wirkert, and Klaus H. Maier-Hein. nnU-Net: Self-adapting Framework for U-Net-Based Medical Image Segmentation. 9 2018.

Qianying Liu, Chaitanya Kaul, Jun Wang, Christos Anagnostopoulos, Roderick Murray-Smith, and Fani Deligianni. Optimizing Vision Transformers for Medical Image Segmentation. 10 2022a.

Ze Liu, Yutong Lin, Yue Cao, Han Hu, Yixuan Wei, Zheng Zhang, Stephen Lin, and Baining Guo. Swin Transformer: Hierarchical Vision Transformer using Shifted Windows. 3 2021.

Zhuang Liu, Hanzi Mao, Chao-Yuan Wu, Christoph Feichtenhofer, Trevor Darrell, and Saining Xie. A ConvNet for the 2020s. 1 2022b.

Bjoern H Menze, András Jakab, Stefan Bauer, Jayashree Kalpathy-Cramer, Keyvan Farahani, Justin S. Kirby, Yuliya Burren, Nicole Porz, Johannes Slotboom, Roland Wiest, Levente Lanczi, Elizabeth R. Gerstner, Marc-André Weber, Tal Arbel, Brian B. Avants, Nicholas Ayache, Patricia Buendia, D. Louis Collins, Nicolas Cordier, Jason J. Corso, Antonio Criminisi, Tilak Das, Hervé Delingette, Çagatay Demiralp, Christopher R. Durst, Michel Dojat, Senan Doyle, Joana Festa, Florence Forbes, Ezequiel Geremia, Ben Glocker, Polina Golland, Xiaotao Guo, Andaç Hamamci,

Khan M. Iftekharuddin, Rajesh Jena, Nigel M. John, Ender Konukoglu, Danial Lashkari, José Antonio Mariz, Raphael Meier, Sérgio Pereira, Doina Precup, Stephen John Price, Tammy Riklin-Raviv, Syed M. S. Reza, Michael T. Ryan, Duygu Sarikaya, Lawrence H. Schwartz, Hoo-Chang Shin, Jamie Shotton, Carlos Alberto Silva, Nuno Sousa, Nagesh K. Subbanna, Gábor Székely, Thomas J. Taylor, Owen M. Thomas, N. Tustison, Gözde B. Ünal, Flor Vasseur, Max Wintermark, Dong Hye Ye, Liang Zhao, Binsheng Zhao, Darko Zikic, Marcel Prastawa, Mauricio Reyes, and Koenraad Van Leemput. The Multimodal Brain Tumor Image Segmentation Benchmark (BRATS). *IEEE Transactions on Medical Imaging*, 34:1993–2024, 2015.

Kyeong Beom Park and Jae Yeol Lee. SwinE-Net: hybrid deep learning approach to novel polyp segmentation using convolutional neural network and Swin Transformer. *Journal of Computational Design and Engineering*, 9:616–632, 4 2022. ISSN 22885048. doi: 10.1093/jcde/qwac018.

Namuk Park and Songkuk Kim. How Do Vision Transformers Work? 2 2022.

Ramprasaath R. Selvaraju, Michael Cogswell, Abhishek Das, Ramakrishna Vedantam, Devi Parikh, and Dhruv Batra. Grad-CAM: Visual Explanations from Deep Networks via Gradient-based Localization. 10 2016. doi: 10.1007/s11263-019-01228-7.

Qixuan Sun, Nianhua Fang, Zhusuo Liu, Liang Zhao, Youpeng Wen, and Hongxiang Lin. HybridCTrm: Bridging CNN and Transformer for Multimodal Brain Image Segmentation. *Journal of Healthcare Engineering*, 2021, 2021. ISSN 20402309. doi: 10.1155/2021/7467261.

Wenxuan Wang, Chen Chen, Meng Ding, Jiangyun Li, Hong Yu, and Sen Zha. TransBTS: Multimodal Brain Tumor Segmentation Using Transformer. In *International Conference on Medical Image Computing and Computer-Assisted Intervention*, 2021.

Zhuofan Xia, Xuran Pan, Shiji Song, Li Erran Li, and Gao Huang. Vision Transformer with Deformable Attention. *2022 IEEE/CVF Conference on Computer Vision and Pattern Recognition (CVPR)*, pages 4784–4793, 2022.

Guoping Xu, Xingrong Wu, Xuan Zhang, and Xinwei He. LeViT-UNet: Make Faster Encoders with Transformer for Medical Image Segmentation. 7 2021.

Hong-Yu Zhou, J. Guo, Yinghao Zhang, Lequan Yu, Liansheng Wang, and Yizhou Yu. nnFormer: Interleaved Transformer for Volumetric Segmentation. *ArXiv*, abs/2109.03201, 2021.